Turkish Journal of Science & Technology
20(2), 465-481, 2025

Research Paper
https://doi.org/10.55525/tjst.1668138

Feeding Analysis of a 79 GHz Phased Microstrip Antenna Array for Autonomous Vehicle Radar Applications

Selen YILMAZ[1], Yaser DALVEREN[2*], Ali KARA[3]

[1] Electrical and Electronics Engineering, Graduate School of Natural and Applied Sciences, Atilim University, Ankara, Türkiye
[2] Electrical and Electronics Engineering, İzmir Bakırçay University, İzmir, Türkiye
[3] Electrical and Electronics Engineering, Gazi University, Ankara, Türkiye
[1] yilmazseleneng@gmail.com, [*2] yaser.dalveren@bakircay.edu.tr, [3] akara@gazi.edu.tr

(Geliş/Received: 02/04/2025; Kabul/Accepted: 23/07/2025)

Abstract: Automotive radar is known as a promising sensing technology in autonomous vehicles due to its reliability. In current autonomous vehicles, the 77 – 81 GHz frequency band is the principal operating band for automotive radars. For the efficient operation of automotive radars, the radar antenna needs to be highly accurate. However, higher operating frequencies may present challenges in radar antenna design, requiring high gain, wide bandwidth, and low sidelobe levels (SLL). To address this issue, this study aims to adapt a planar series-fed linear antenna array to 79 GHz automotive radar applications using three different grounded coplanar waveguide (GCPW) feed configurations, including coplanar gap source port, vertical ground bridge, and wave port. Simulations were conducted to evaluate the performance of the antenna with the feed configurations. According to the results, it was shown that the antenna with wave port feed achieved the best impedance bandwidth (>3 GHz), whereas the antenna with either the coplanar gap source port or the vertical ground bridge configurations exhibited better main lobe phase centering and a higher gain (>18.4 dBi), with an acceptable SLL below −16.28 dB. It is believed that these findings may contribute to the development of high-performance radar antennas for next-generation autonomous vehicles.

Key words: Autonomous vehicles, radar, microstrip antenna, antenna feed, array antenna, feeding analysis.

Otonom Araç Radarları için 79 GHz Fazlı Mikroşerit Anten Dizisinin Besleme Analizi

Öz: Otomotiv radarı, güvenilirliği nedeniyle otonom araçlarda umut vadeden bir algılama teknolojisi olarak bilinmektedir. Günümüz otonom araçlarında, 77 – 81 GHz frekans bandı otomotiv radarları için ana çalışma bandıdır. Otomotiv radarlarının verimli çalışabilmesi için radar anteninin son derece hassas olması gerekir. Ancak, yüksek çalışma frekansları, yüksek kazanç, geniş bant genişliği ve düşük yan lob seviyeleri (SLL) gerektiren radar anteni tasarımında zorluklar ortaya çıkarabilmektedir. Bu sorunu ele almak için, bu çalışmada, eş düzlemli boşluk kaynak portu, dikey toprak köprüsü ve dalga portu dahil olmak üzere üç farklı topraklanmış eş düzlemli dalga kılavuzu (GCPW) besleme konfigürasyonu kullanılarak düzlemsel seri beslemeli doğrusal bir anten dizisinin 79 GHz otomotiv radar uygulamalarına uyarlaması amaçlanmaktadır. Antenin besleme yapılandırmalarıyla performansını değerlendirmek için benzetimler yürütülmüştür. Elde edilen sonuçlara göre, dalga portu beslemeli antenin en iyi empedans bant genişliğini (>3 GHz) elde ettiği, eş düzlemli boşluk kaynak portu veya dikey toprak köprüsü konfigürasyonları beslemeli antenin ise daha iyi ana lob faz merkezlemesi ve daha yüksek bir kazanç (>18,4 dBi) sergilediği, yan lob seviyelerinin (SLL) −16,28 dB'nin altında olduğu gösterilmiştir. Bu bulguların, yeni nesil otonom araçlar için yüksek performanslı radar antenlerinin geliştirilmesine katkıda bulunabileceği düşünülmektedir.

Anahtar kelimeler: Otonom araçlar, radar, mikroşerit anten, anten beslemesi, dizi anten, besleme analizi.

1. Introduction

Road traffic accidents are one of the leading causes of all deaths worldwide. The world health organization (WHO) has announced that over 1.2 million deaths worldwide in 2016 were caused by road traffic accidents [1]. Recently, in order to provide safer roads, intelligent transportation systems (ITS) based on the Internet-of-Things (IoT) have been appeared [2]. Moreover, the advanced driver assistance system (ADAS) for IoT-based ITS has also been emerged to reduce accidents and causalities [3]. Mainly, the functions of ADAS can be categorized into two groups: (a) safety functions and (b) comfort functions. In comfort functions, the driver is warned to avoid accidents. In safety functions, the vehicle itself is triggered in the event that the driver does not react to a dangerous

* Corresponding author: yaser.dalveren@bakircay.edu.tr. ORCID Number of authors: [1] 0000-0003-0179-559X, [2] 0000-0002-9459-0042, [3] 0000-0002-9739-7619

situation. Therefore, due to its many useful features, ADAS is becoming increasingly popular. Nowadays, its functions are being taken over by the automotive industry to develop autonomous vehicles.

Accurate environmental sensing and the implementation of intelligent decision-making are two critical requirements for the realization of autonomous driving. The aim of sensing is to provide accurate information by monitoring the surroundings of an autonomous vehicle. More specifically, all information regarding the vehicle's path on the road is acquired, and then, the obstacles are detected and timely reported to safely plan the route. Hence, in autonomous driving, the use and performance of multiple integrated sensors in autonomous vehicles have an important role [4]. Generally, autonomous vehicles are equipped with three key types of sensors, such as cameras [5], light detection and ranging (lidar) [6], and radio detection and ranging (radar) [7]. Cameras are not able to provide target range and velocity estimation, and they are vulnerable to bad weather and poor lighting conditions. Thus, radars or lidars are mostly preferred for an automotive sensing suit [8]. On the other hand, the use of lidars in automotive vehicles is limited due to their lower reliability, higher cost, and integration challenges [9]. Therefore, low-cost, high-resolution, and reliable automotive radars become an effective choice for sensing purposes in autonomous vehicles [10].

Typically, an automotive radar consists of a transceiver that contains both a transmitter and a receiver. Within the transmitter, the generated and modulated signal is directed towards the target through a radio frequency component, known as a transmitting antenna. In the receiver, the echoes returned from the target are collected via a receiving antenna. This is followed by down-conversion, filtering, and sampling processes to achieve the baseband signal, which is further processed for target detection. Evidently, the antenna is one of the important RF components in a typical automotive radar system. Therefore, an automotive radar antenna should be able to provide high accuracy for ensuring an efficient radar operation.

An automotive radar system are required to possess the capability of operating effectively in dense scattering environments like urban areas. As is widely known, these environments are characterized by a huge number of reflecting objects that are closely spaced. This means that higher range resolution is required not only to estimate the position of the targets but also to distinguish them accurately [11], [12]. Hence, the requirement of higher range resolution leads to demands on the use of higher operating frequencies with wider bandwidths. In this context, early automotive radars were operated at 24 GHz with a 250 MHz bandwidth, providing a range resolution of 0.75 m. Nevertheless, due to the demand for increased operating frequencies and enhanced range resolution, automotive radars have started to use higher operating frequencies and bandwidth that provide an approximate range resolution of 4 cm. Accordingly, the 77 – 81 GHz frequency range becomes the principal operating band for automotive radars in current autonomous vehicles [13].

High operating frequencies can degrade the performance of automotive radar antennas. In general, an automotive radar antenna is expected to exhibit high gain, wide bandwidth, and low sidelobe levels (SLL), while also maintaining low cost and compact dimensions for ease of fabrication. Considering these performance parameters and design constraints, numerous studies have focused on automotive radar antenna designs operating at 79 GHz [14]-[30]. The predominant approach in these studies has been to enhance gain and narrow beamwidth. However, as previously highlighted, employing higher operating frequencies with wider bandwidths is crucial for achieving high range resolution in automotive radars.

Among the existing 79 GHz designs, the antenna proposed in [30] reports the highest peak gain, approximately 18.12 dBi, along with the operational bandwidth of 1.5 GHz and a SLL of −20 dB. However, due to its complex structure, the requirement of manufacturing simplicity cannot be satisfied. Thus, the inherent structural complexity of this design may impede its manufacturability. This limitation identifies a research gap concerning the development of simplified, high-gain antennas optimized for 79 GHz automotive radar applications. To bridge this gap, this study aims to adapt the planar series-fed linear antenna array proposed in [31] to operate at 79 GHz by implementing different antenna feed configurations. Specifically, the performance of the planar series-fed linear antenna was evaluated using three grounded coplanar waveguide (GCPW) feed configurations, including coplanar gap source port, vertical ground bridge, and wave port. In this context, full-wave electromagnetic field simulations were conducted using high-frequency structure simulator (HFSS). The simulation results demonstrated that the wave port-fed antenna achieved the best impedance bandwidth (>3 GHz), while the other two configurations provided better main lobe phase centering and higher gain (>18.4 dBi) with SLL values around −16.28 dB.

The rest of the paper is organized as follows. In Section 2, automotive radar antenna designs operating at 79 GHz are briefly discussed to address the main contributions of this study. This is followed by Section 3 where the design of the planar series-fed linear antenna array is given. Then, in Section 4, the antenna feed configurations are described. Next, simulation results are presented in Section 5. In Section 6, the results are comparatively assessed, and suggestions for the future work are addressed. Finally, the paper is concluded in Section 7.

2. Overview of Antennas for Automotive Radar at 79 GHz

Basically, automotive radar systems are classified into three types, namely long-range radars (LRRs), medium-range radars (MRRs), and short-range radars (SRRs). Since LRRs can be implemented to detect far-field objects at around 250 m, they are widely used for adaptive cruise control. MRR and SRR can be implemented to detect medium- or short-field objects from 1 to 60 m, which are mainly used for blind spot detection or parking assistance. Today, because of their simplicity, frequency-modulated continuous-wave (FMCW) radars are also used in autonomous vehicles for high-resolution measurements [32]. Both radar types can operate higher frequency bands (76-81 GHz) in order to achieve broader detection range with higher range resolution. For this reason, the design of a simple and cost-effective radar antenna operating at 79 GHz that provides high gain, wide bandwidth, and low SLL becomes significant issue for next-generation autonomous vehicles. To address this issue, several antenna designs have been proposed in the literature [14]-[30].

In [14], a microstrip patch array antenna based on low-temperature co-fired ceramics (LTCC) technology is presented. The antenna exhibits an impedance bandwidth of approximately 5 GHz and a maximum gain of 13 dBi. In [15], a hybrid thin-film antenna is proposed, with its performance evaluated using three different feed networks based on substrate-integrated waveguide (SIW), GCPW, and microstrip transmission lines. The maximum impedance bandwidth is recorded as 11.3 GHz for both the GCPW- and microstrip-fed antennas, while the highest gain is measured at 12.1 dBi, with a minimum sidelobe suppression of 18 dB for the MS-fed configuration. In [16], an integrated lens antenna incorporating a six-layer cylindrical Luneburg lens and a 17-element planar leaky-wave periodic dipole (PLPD) array, fed by SIW and microstrip lines, is introduced. The reported maximum gain and bandwidth are 13.05 dBi and 7 GHz, respectively, with the worst sidelobe level measured at -16.35 dB. In [17], a patch antenna array utilizing an inset-feeding line is proposed, achieving a gain of 12.1 dBi and a bandwidth of 1.21 GHz. In [18], a planar grid array antenna is introduced, demonstrating a peak gain of approximately 16 dB, while the sidelobe level (SLL) remains below -13 dB. In [19], a compact grid antenna array designed for millimeter-wave radar (MRR) applications is presented, with a reported gain of 13.52 dBi and an SLL of -14 dB. Additionally, the antenna achieves a bandwidth of 9.6 GHz. In [20], a wideband microstrip comb-line antenna array is described, exhibiting a gain of 12.36 dB and a sidelobe suppression greater than 15 dB, with an achieved bandwidth of 12 GHz. In [21], a proximity-coupled feed patch antenna array is proposed, featuring a gain of 14.8 dB and a bandwidth of 5.5 GHz. In [22], a patch array antenna employing a double indirect-coupled feeding structure is introduced. Experimental results indicate an average gain of 11.5 dBi and a bandwidth of 5 GHz, with a maximum SLL of -15.9 dB. In [23], a microstrip corporate center-fed antenna is presented, achieving a gain of approximately 12 dB, a bandwidth of 5 GHz, and an SLL of less than -20 dB. In [24], a double-layer broadband microstrip antenna with a wide beam is proposed, exhibiting a gain of approximately 11 dB, a bandwidth of 5 GHz, and an SLL below -20 dB. In [25], a multilayer series-fed patch antenna array incorporating stacked micro-via loading is designed. The maximum gain is reported as 12.67 dBi, while the measured bandwidth reaches 7.5 GHz, with sidelobe suppression exceeding 12.9 dB. In [26], a three-dimensional (3D) mold-embedded printed circuit board (PCB)-based multiple-input multiple-output (MIMO) antenna array is introduced. The results demonstrates a peak gain of 11.7 dBi and an impedance bandwidth of at least 3 GHz. In [27], an SIW slot-coupled patch antenna is proposed. It yields a measured gain of 11.29 dBi and a bandwidth of approximately 7 GHz. In [28], a wideband cavity-slotted waveguide antenna is presented. It achieves an extensive bandwidth of 22 GHz and an antenna gain of 14.5 dBi. Furthermore, the lowest observed SLL is approximately -25 dB. In [29], a castle-shaped dielectric resonator antenna with a coplanar waveguide (CPW) feed is designed. It exhibits a bandwidth of 5 GHz and a peak gain of 11.5 dB. In [30], a sector beam transmit antenna employing series-fed microstrip patch arrays with phase-adjusting power dividers is developed for use in short-range radar (SRR) sensors. Additionally, a linear patch antenna array is proposed to enhance detection accuracy. The implementation of the radar system results in a bandwidth of 1.5 GHz and a peak gain of 18.12 dBi.

As a summary, the antennas operating at 79 GHz designed for automotive radars are listed in Table 1. When the antennas are compared in terms of high gain, wide bandwidth, and low SLL, the sector beam antenna proposed in [30] exhibit better performance. Specifically, it demonstrates the highest peak gain, achieving approximately 18.12 dBi, with an operational bandwidth of 1.5 GHz and a SLL of −20 dB. Nevertheless, its complex structure poses significant challenges in terms of manufacturing simplicity. To address this issue, this study aims to adapt the planar series-fed linear antenna array proposed in [31] for operation at 79 GHz by exploring various antenna feed configurations.

Table 1. Comparison of the 79 GHz antenna designs.

Ref.	Antenna Type	Gain (dBi)	Bandwidth (GHz)	SLL (dB)
[14]	Microstrip patch array	13	5	*
[15]	Hybrid thin film with MS feed	12.1	11.3	−18
[16]	Lens antenna	13.05	7	−16.35
[17]	Patch array	12.1	1.21	-
[18]	Planar grid array	16	4	−13
[19]	Compact grid array	13.52	9.6	−14
[20]	Comb-line array	12.36	12	−15
[21]	Proximity-coupled feed patch antenna	14.8	5.5	*
[22]	Patch array antenna using a double indirect coupled feeding structure	11.5	5	−15.9
[23]	Microstrip corporate center-fed antenna	12	5	−20
[24]	Double-layer microstrip antenna	11	5	−20
[25]	Multilayer series-fed patch antenna array	12.67	7.5	−12.9
[26]	3D mold embedded PCB-based multiple MIMO antenna array	11.7	3	*
[27]	SIW slot-coupled patch antenna	11.29	7	*
[28]	Cavity-slotted waveguide antenna	14.5	22	−25
[29]	CPW-fed castle shaped dielectric resonator antenna	11.5	5	*
[30]	Sector beam antenna	18.12	1.5	−20

*: Not provided.

3. Antenna Design

3.1. Design of Single Array Element at 79 GHz

Using a grounded, thin substrate enables to suppress or significantly minimize parasitic surface waves at millimeter-wave frequencies, which enhances radiated power efficiency [33]. To achieve this, the antenna was designed on a single-layer Rogers RO3003 substrate with a thickness of 0.127 mm (5 mil), a relative permittivity of $\varepsilon_r = 3$, and a dielectric loss tangent of 0.0013. The dielectric substrate is fully grounded on its backside, with dimensions of 25 mm in width and 45 mm in length.

For the initial theoretical dimension estimations, the transmission-line model analysis was employed before performing full-wave electromagnetic simulations in HFSS. This approach enables calculation of patch dimensions and the effective dielectric constant to ensure optimal radiation efficiency. The model comprises two slots and a transmission line. In the context of the microstrip antenna, the slots are separated by a transmission with a length (L), width (W) and a characteristic impedance (Z_c). The transmission line is positioned on a dielectric substrate with height (h) and an electrical permittivity (ε_r). The slots of the patch at each end have high impedance, which cause the edges to act as an open circuit. Therefore, the patch exhibits a significantly resonant characteristic

as a function of its L. Since the field lines at the edges of the patch are exposed to the fringing effect, the patch may appear electrically larger than its physical size. The fringing fields propagate through a non-homogeneous dielectric medium, specifically the substrate and air interface. The distribution of electromagnetic energy between the substrate and air regions is dependent on the patch length-to-substrate height ratio (L/h), the patch width-to-substrate height ratio (W/h), and the substrate's relative permittivity (ε_r). The resulting non-uniform field distribution results in the excitation of a quasi-transverse electromagnetic (quasi-TEM) mode, rather than a pure TEM mode, due to differing phase velocities in air and substrate regions. Hence, a pure TEM mode is unattainable in practical microstrip structures. Furthermore, increasing the substrate thickness enhances the fringing effect. This may then lead to a greater difference between the physical and electrical dimensions of the patch edges and a reduction in the resonant frequency. Therefore, accurate characterization of the electromagnetic behavior in the presence of fringing fields necessitates the computation of an effective dielectric constant (ε_{eff}). Figure 1 illustrates a typical microstrip transmission line.

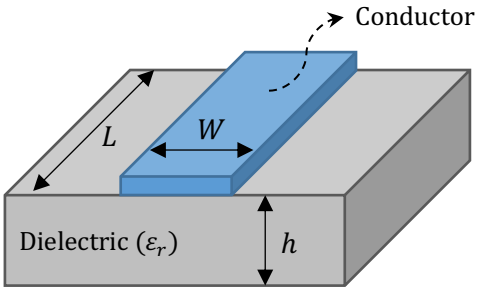

Figure 1. Microstrip transmission line.

The effective dielectric constant (ε_{eff}) lies within the range $1 < \varepsilon_{eff} < \varepsilon_r$. When the substrate permittivity is significantly greater than one ($\varepsilon_r \gg 1$), as is typically the case, ε_{reff} approaches the actual permittivity value. Moreover, the effective dielectric constant is dependent on the operating frequency. At higher operating frequencies, a greater proportion of the electric field is confined within the substrate, causing the transmission line to behave like a homogeneous medium. Then, since the resonance frequency increases, ε_{eff} converges toward the actual dielectric constant of the substrate. For $W/h > 1$, the effective dielectric constant can be calculated as expressed in Equation (1) [34]:

$$\varepsilon_{eff} = \frac{\varepsilon_r+1}{2} + \frac{\varepsilon_r-1}{2}\left(1 + 12\frac{h}{W}\right)^{-0.5}. \quad (1)$$

In microstrip antenna design, fringing fields at the patch edges contribute to an increased electrical length relative to the physical dimensions. This effect demonstrates as an extension of the resonant patch by ΔL along both sides, which is crucial for accurate resonance frequency prediction, as illustrated in Figure 2.

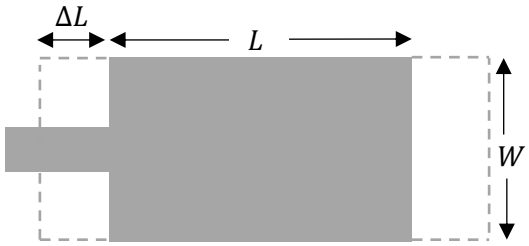

Figure 2. Frontal view of patch antenna illustrating edge effects.

Then, the length extension ΔL of the patch can be calculated as given in Equation (2) [34]:

$$\Delta L = 0.412h\frac{(\varepsilon_{reff}+0.3)\left(\frac{W}{h}+0.264\right)}{(\varepsilon_{reff}-0.258)\left(\frac{W}{h}+0.8\right)}. \quad (2)$$

Given the extension occurs along both edges of the patch, the effective resonant length can be calculated as stated in Equation (3) [34]

$$L_{eff} = L + 2\Delta L\,. \quad (3)$$

In order to calculate the resonance frequency of a rectangular cavity (f_{rc}), it is essential to incorporate the patch length and edge effects. For the transverse magnetic (TM_{010}) mode excitation, the resonance frequency is given by Equation (4) [34]

$$(f_{rc})_{010} = q\frac{c}{2L\sqrt{\varepsilon_r}} = \frac{c}{2L_{eff}\sqrt{\varepsilon_{eff}}}, \quad (4)$$

where c is the speed of light, and q is defined as the fringe factor.

Lastly, the approximate width of the patch can be determined by Equation (5) [34]

$$W = \frac{c}{2f_r}\sqrt{\frac{2}{\varepsilon_r+1}}. \quad (5)$$

where f_r is the operating (resonant) frequency.

3.2. Phase Shift Calculation and Phase Correction

As previously mentioned, this study aims to shift the antenna resonance frequency from 76.5 GHz to 79 GHz. Consequently, the reduction in guided wavelength leads to an increase in phase delay between consecutive array elements. This, in turn, results in a degradation of directivity and an increase in the SLL. To ensure that all array elements radiate in phase at the primary operating frequency of 79 GHz, phase shifts between successive elements are computed using Equation (6) [35]

$$\Delta\varphi = \frac{2\pi d\sin\theta_s}{\lambda_g}, \quad (6)$$

where d represents the spacing between adjacent elements, θ_s denotes the main lobe steering angle, λ_g is the guided wavelength within the substrate, and $\Delta\varphi$ corresponds to the phase delay between two successive array elements. Based on Equation (6), inter-element spacings are uniformly scaled down by a constant factor to mitigate undesired phase shifts within the linear array. Furthermore, the lengths of all array elements are adjusted according to the actual values derived from transmission line model analysis. As a result, the main beam is designed to be centered at $\theta = 0^{o}$ in the E-plane at 79 GHz.

3.3. Antenna Configuration

The top view of the antenna array design is presented in Figure 3. In this configuration, the number of array elements is set to $N = 16$ to ensure compatibility with automotive LRR and MRR. This selection is based on the well-established principle that increasing the number of array elements proportionally enhances directivity while simultaneously reducing the 3 dB beamwidth across the entire array. Thus, a linear array with a higher number of elements results in a more focused and directive main beam. Notably, to achieve a low SLL, the Dolph-Chebyshev amplitude tapering technique is widely employed, as it enables the minimization of SLL for a given beamwidth [36], [37]. This approach is also adopted in this study.

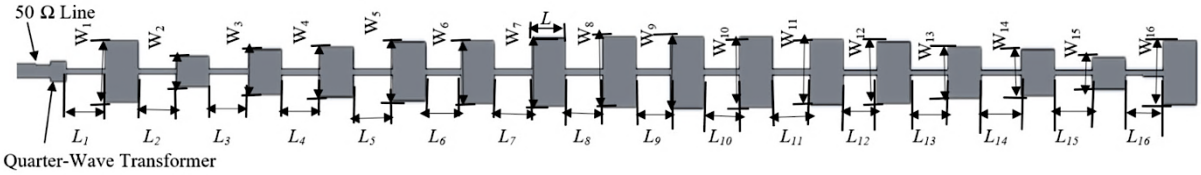

Figure 3. Illustration of the antenna array (top-view).

Since the primary focus of this study is the E-plane radiation pattern (at $\Phi = 90^{o}$), all dimensions along the axis on which the array elements are sequentially arranged have been optimized according to the feeder configurations outlined in the following section. The patch width dimensions ($W_1, \ldots, W_{16}$) along the H-plane (at $\Phi = 0^{o}$) are used as specified in Table 2 due to their negligible impact on the overall antenna performance. However, the interelement spacing lengths ($L_1, \ldots, L_{16}$) are varied depending on the antenna feed configurations.

Table 2. Patch width values (in mm) [31].

Parameter	Value	Parameter	Value	Parameter	Value	Parameter	Value
W_1	1.22	W_5	1.19	W_9	1.45	W_{13}	1.05
W_2	0.62	W_6	1.27	W_{10}	1.42	W_{14}	0.93
W_3	0.90	W_7	1.38	W_{11}	1.31	W_{15}	0.65
W_4	1.00	W_8	1.40	W_{12}	1.24	W_{16}	1.3

3.4. Ground-Signal-Ground Transition Structure

A transition structure is essential for establishing a connection between the stripline of the radiating patch and the waveguide, particularly when operating at very high or ultra-high frequencies. For on-wafer measurements, a properly designed GCPW can improve impedance matching and suppress parasitic higher-order modes. Accordingly, the width of the ground pads and the total CPW width can be optimized as given in Equation (8) [38]

$$W_{\text{total}} < \frac{2c}{f_{max}\sqrt{2(\varepsilon_r - 1)}}, \tag{8}$$

where f_{max} denotes the upper limit of the operating frequency band, and W_{total} represents the total coplanar waveguide width. The GSG stripline-to-coplanar waveguide transition structure, along with the optimized dimensions, is depicted in Figure 4, where $W_g = 1.4$ mm, $S = 40$ μm, and $W_s = 0.12$ mm. Here, the sum of W_g, S, and W_s corresponds to W_{total}.

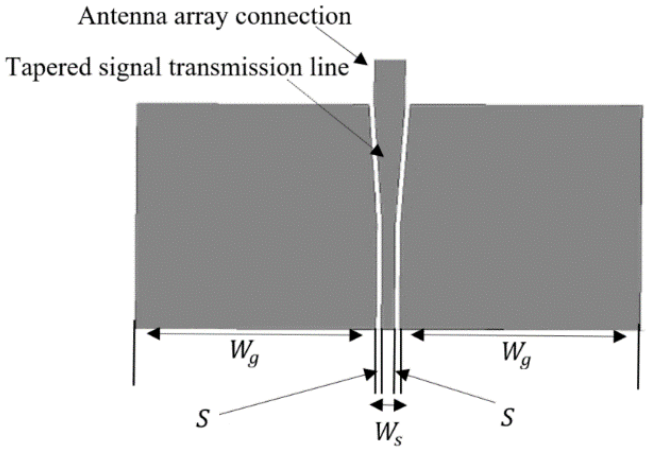

Figure 4. The geometry of the GSG padding (top-view).

The length of the tapered transmission line length is set to $3\lambda_g/4$ is based on transmission line theory to ensure accurate impedance matching between the waveguide probe and the 50 Ω feed line. Furthermore, the length of the waveguide probe connecting line is optimized to introduce a phase shift of approximately 180º.

As a result, in accordance with the variations in guided wavelength relative to [31], a scaling method with optimized scale factor values is employed. Patch dimensions and inter-element spacings are approximated to $0.5\lambda_g$ at 79 GHz, scaled according to the decrease in guided wavelength. This ensures in-phase excitation of all elements at the center frequency of 79 GHz. Additionally, the lengths of the quarter-wave transformer and 50 Ω feed line are optimized for the reduced operating wavelength, as shown in Figure 3.

4. Antenna Feed Configurations

At higher frequencies, GCPW offers several advantages that make it a reasonable choice in comparison to other feeding options, such as microstrip lines and SIW. Moreover, it facilitates the easy mounting of both shunt and series components, simplifying circuit design and integration. Thus, GCPW provides a good balance of performance, ease of fabrication, and integration, making it a suitable choice for many high-frequency antenna applications. In this study, therefore, three GCPW feed configurations are proposed to adapt the antenna array described in the previous section for an efficient operation at 79 GHz: (a) a coplanar gap source port, (b) a vertical ground bridge, and (c) a wave port. The following sections provide an overview of the fundamental characteristics of these configurations along with their simulation details.

4.1. Feed Configuration 1: Coplanar Gap Source Port

Coplanar gap source port is a technique employed to introduce electromagnetic energy into CPW structures by creating a discontinuity, or gap, within the signal conductor. This gap acts as a localized impedance mismatch, allowing for the application of an external source. The fundamental principle relies on the generation of an electric field (E-field) across the gap when a source port, modeled as a voltage or current source, is applied. According to Faraday's law, this E-field induces a magnetic field (H-field), initiating the propagation of electromagnetic waves along the CPW. The dimensions of the gap width directly affect the source impedance and excitation efficiency. Optimizing the gap design is crucial for achieving a suitable impedance match and maximizing power transfer.

In simulations, the source port is typically modeled using lumped or wave port. Lumped ports represent voltage or current sources applied across the gap, while wave ports are more suitable for modeling guided wave structures. By controlling the gap dimensions, source port characteristics, and considering the substrate properties, coplanar gap source port provides an effective method for analyzing and optimizing CPW-based devices.

Figure 5 shows the coplanar gap source feed as the first feed configuration proposed in this study. This configuration employs lumped port assigned to a coplanar rectangular sheet to top of substrate connecting the joined side ground pads to the central signal trace.

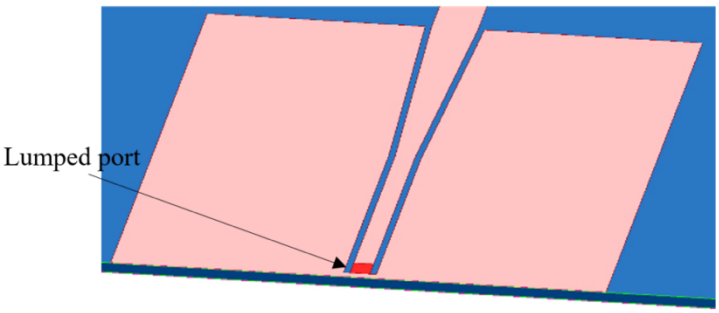

Figure 5. Coplanar gap source port.

4.2. Feed Configuration 2: Vertical Ground Bridge

A vertical or horizontal ground bridge is a commonly used method for representing on-wafer GSG waveguide probe measurements. When appropriately designed within a three-dimensional full-wave electromagnetic field solver, this setup enables simulations to accurately approximate experimental measurement results [39].

The configuration used in this study consists of a vertical perfect electric conductor (PEC) bridge to short the two side ground pads and to maintain them at the same potential. A lumped port is assigned to a vertical rectangular sheet positioned between the central signal trace and the PEC bridge. Both the lumped port and the bridge are precisely perpendicular to the GSG padding.

In accordance with the direction of current flow, the integration line of the lumped port is defined from the PEC bridge toward the signal trace. To minimize the parasitic inductance induced by the height of the PEC bridge, the bridge height is optimized and calibrated. Additionally, the lumped port is designed as a square sheet to mitigate parasitic capacitance. The excitation scheme is shown in Figure 6.

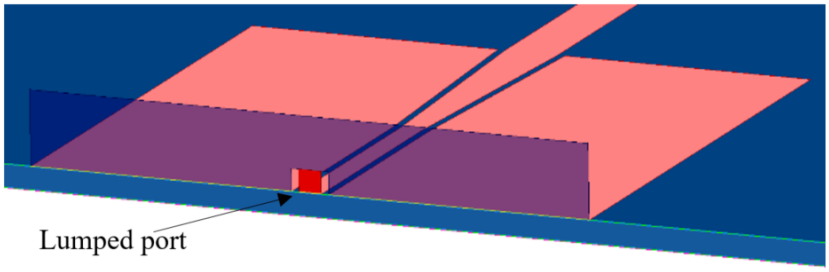

Figure 6. Vertical ground bridge.

4.3. Feed Configuration 3: Wave Port

The final configuration employs a conventional wave port feed applied to the antenna array. To ensure accurate generation of electromagnetic fields, the wave port needs to be sufficiently wide and tall to confine the energy between the line and ground pads. However, excessively large dimensions (exceeding $\lambda_g/2$ in any port component) can induce rectangular waveguide modes. Therefore, it is necessary to select the width and height of the wave port carefully. In this context, the propagation constant within the operating bandwidth should be examined to identify any potential parasitic higher-order mode resonances. Figure 7 presents the designed simulation structure incorporating the wave port.

Figure 7. Wave port excitation.

5. Simulation Results

Electromagnetic simulations were performed in HFSS to evaluate effects of the feed configurations on the performance of the 1×16 microstrip patch antenna array at 79 GHz. Before conducting the simulations, the interelement spacing lengths shown in Figure 3 ($L_1, \ldots, L_{16}$) were determined based on the feed configuration, as listed in Table 3, to be used in the antenna array design. In the table, the lengths considered for the antenna design in [31] are also provided for comparison.

Table 3. Interelement spacing lengths (in mm) for the antenna array with the feed configurations.

Parameter	Value		
	[31]	Feed Configuration 1 & 2	Feed Configuration 3
L_1	1.2400	1.1904	1.2028
L_2	1.2000	1.1520	1.1640
L_3	1.2500	1.2000	1.2125
L_4	1.2400	1.1904	1.2028
L_5	1.2500	1.2000	1.2125
L_6	1.1500	1.1040	1.1155
L_7	1.2000	1.1520	1.1640
L_8	1.2000	1.1520	1.1640
L_9	1.1000	1.0560	1.0670
L_{10}	1.1500	1.1040	1.1155
L_{11}	1.2000	1.1520	1.1640
L_{12}	1.0800	1.0368	1.0476
L_{13}	1.2000	1.1520	1.1640
L_{14}	1.3000	1.2480	1.2610
L_{15}	1.2000	1.1520	1.1640
L_{16}	1.2000	1.1520	1.1640

5.1. Antenna with Feed Configuration 1

Figure 8 presents the simulated reflection coefficient ($|S_{11}|$) and gain of the antenna array with the first feed configuration as a function of frequency. The $|S_{11}|$ response exhibits a sharp resonance around 78.8 GHz, where it reaches a minimum value of approximately -22.6 dB that indicates excellent impedance matching and minimal power reflection. The operational (impedance) bandwidth, typically defined as the frequency range where $|S_{11}|$ remains below -10 dB, extends approximately from 78.28 GHz to 79.61 GHz, yielding a bandwidth of 1.33 GHz. This broad bandwidth is critical for high-resolution radar applications. Moreover, the gain remains relatively stable across the frequency range. The maximum gain within the operating band reaches up to 18.416 dBi at 78.85 GHz, exhibiting a maximum deviation of 0.39 dBi throughout the entire resonance band.

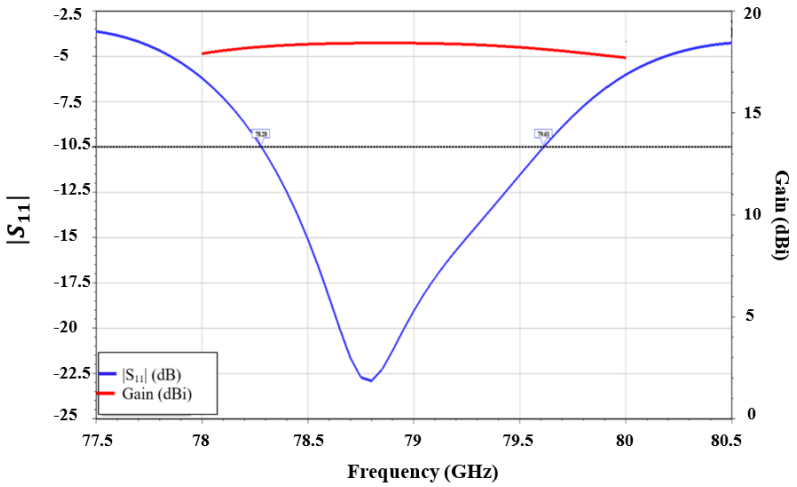

Figure 8. Simulated results of $|S_{11}|$ and gain results for the first feed configuration.

Figure 9 shows the simulated E-plane radiation pattern of the patch antenna array with the first feed configuration at a frequency of 79 GHz. The gain is plotted as a function of the scanning angle (θ) at $\Phi = 90^{o}$, representing the principal plane radiation characteristics. The SLL is observed at approximately less than -15.4 dB with half-power beamwidth (HPBW) of 5.753°. This suppression is crucial in reducing interference from unwanted directions, thereby improving the signal-to-noise ratio (SNR) in radar applications.

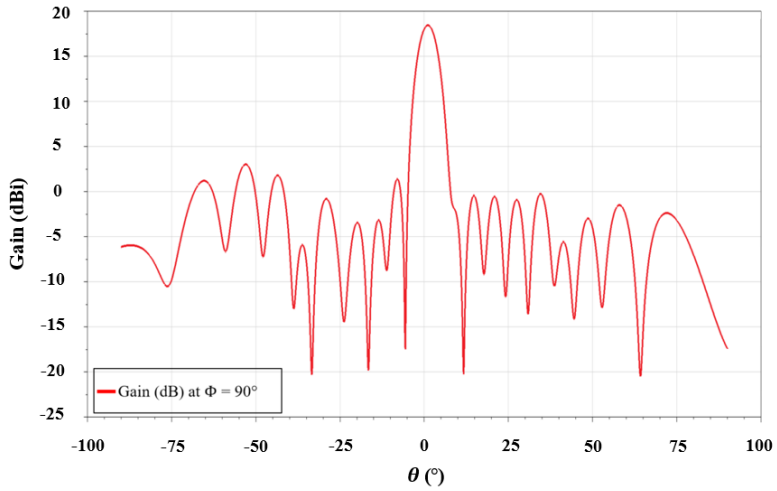

Figure 9. E-plane radiation pattern at 79 GHz for the first feed configuration.

5.2. Antenna with Feed Configuration 2

Figure 10 presents the simulated $|S_{11}|$ and gain characteristics under bridge excitation. From the results, a -10 dB impedance bandwidth of 1.39 GHz, spanning the frequency range from 78.37 GHz to 79.76 GHz, can be clearly observed. This bandwidth enables to maintain effective signal transfer within the designated operational band. Furthermore, the peak gain within the band reaches 18.435 dBi at 79 GHz, indicating significant signal amplification. The gain exhibits a maximum deviation of 0.41 dBi across the entire bandwidth, which suggests a stable and consistent amplification profile.

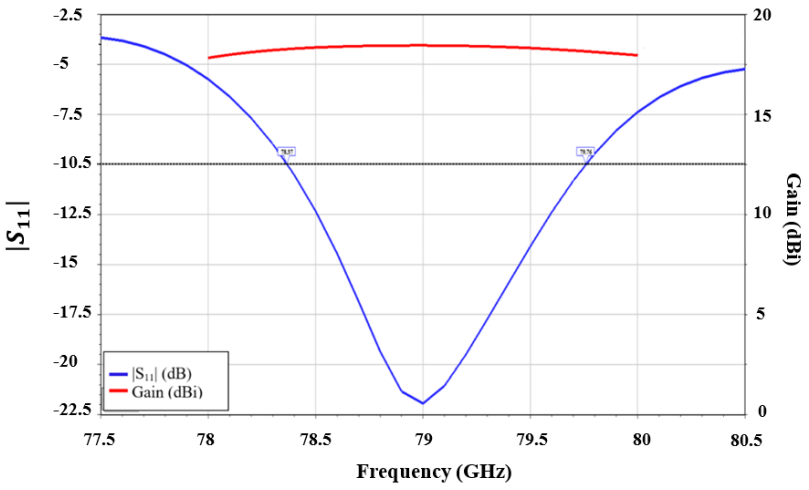

Figure 10. Simulated results of $|S_{11}|$ and gain results for the second feed configuration.

To further assess the radiation characteristics, Figure 11 illustrates the E-plane radiation pattern at 79 GHz. Furthermore, the SLL is maintained below -16.28 dB, signifying minimized interference and enhanced directivity.

The HPBW is approximately 5.7º, which indicates a highly focused radiation pattern. This, in fact, is crucial for targeted signal transmission and reception.

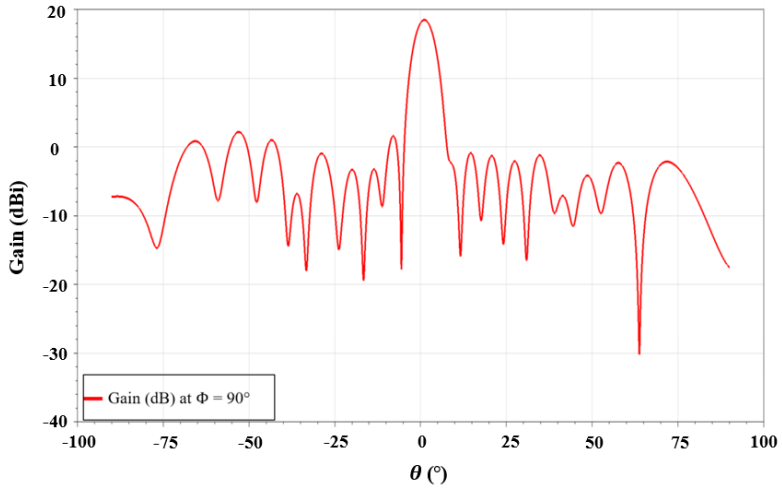

Figure 11. E-plane radiation pattern at 79 GHz for the second feed configuration.

5.3. Results of Feed Configuration 3

The simulated $|S_{11}|$ and gain of the antenna array with the third feed configuration are shown in Figure 12. From the results, a -10 dB impedance bandwidth of 3.05 GHz is observed, which cover the frequency range from 78.95 GHz to 82 GHz. Moreover, the peak gain achieves 17 dBi at 81.05 GHz. The gain variation across the resonance band is limited to a maximum deviation of ~0.62 dBi, which indicates a stable and consistent amplification profile.

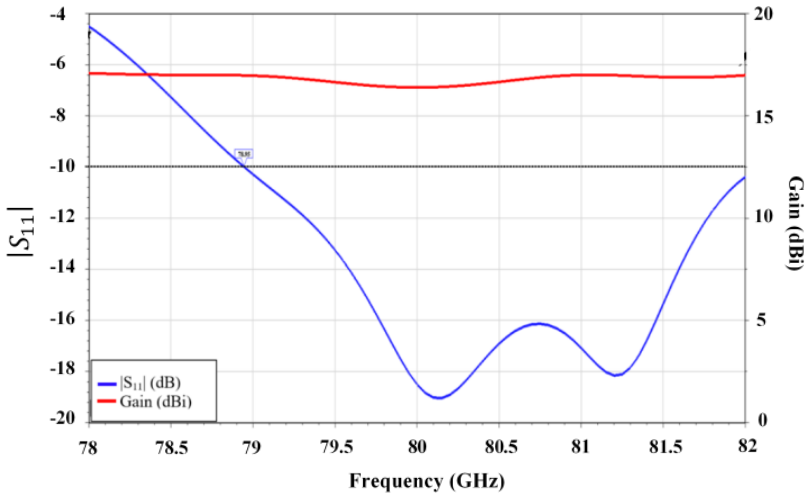

Figure 12. Simulated results of $|S_{11}|$ and gain results for the third feed configuration.

To further analyze the radiation characteristics, Figure 13 presents the E-plane radiation pattern at 79 GHz. The SLL is observed below -15 dB, which indicates the effective suppression of unwanted radiation and enhanced directivity. Additionally, a HPBW of approximately 5.7º is observed.

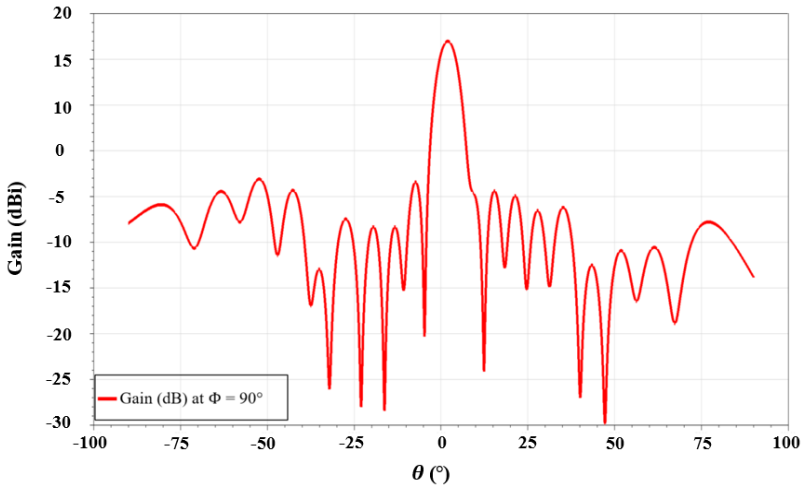

Figure 13. E-plane radiation pattern at 79 GHz for the third feed configuration.

6. Discussion

The results achieved from the simulations demonstrate the effects of various GCPW feed configurations on the antenna's performance characteristics. The first two configurations (coplanar gap source port and vertical ground bridge) utilize a lumped port, whereas the third (wave port) employs a wave port. In general, wave ports serve as sources of TEM or quasi-TEM mode waves. As is known, a wave port can be represented as a 2D terminal face or, when backed by a 3D PEC object, as part of a semi-infinitely long waveguide with a cross-section matching that of the port. This configuration allows wave ports to support multiple propagating modes. In contrast, lumped ports emulate a current sheet source and function as a lumped RLC (resistor-inductor-capacitor) circuit element, supporting only single-mode propagation. Wave ports allow computation of complex propagation constants and identification of higher-order modes, unlike lumped ports. Based on these fundamental differences, the effects of three GCPW feed configurations on the antenna performance could be evaluated.

To provide an overall comparison between the feed configurations, the E-plane radiation patterns and the simulated $|S_{11}|$, and the gain characteristics of the configurations are shown in Figure 14, Figure 15, and Figure 16, respectively. From the simulation results, distinct differences are observed between the lumped port and wave port configurations, particularly in terms of $|S_{11}|$ and main lobe phase correction within the E-plane radiation pattern at the center frequency of 79 GHz. More specifically, the antenna with a wave port, achieves a wider impedance bandwidth exceeding 3 GHz, compared to approximately 1.4 GHz for the first two configurations utilized lumped ports. However, the antenna with wave port configuration exhibits a frequency shift of approximately 0.6 GHz toward a higher frequency range, whereas the lumped port fed antennas demonstrate better convergence to the target center frequency of 79 GHz. Additionally, analysis of the E-plane radiation pattern reveals that the lumped port fed antennas offer improved main lobe phase centering at $\theta = 0^{o}$ at 79 GHz compared to the wave port fed antenna. Specifically, the antenna with lumped port exhibits a main lobe tilt of $\theta = 1.1^{o}$, while the wave port feed results in a larger shift of $\theta = 1.94^{o}$ at the same frequency. It is important to note that high directivity is a desirable characteristic for automotive radar applications, as it enhances the antenna's ability to focus energy in a specific direction for improved target detection and resolution. Furthermore, the first and second feed configurations are highly correlated to each other and achieve gains exceeding the 18.4 dBi reported in [31] within the adjusted operating band.

On the other hand, the sector beam antenna presented in [30] exhibits a peak gain of 18.12 dBi, whereas the antenna with lumped port-fed configuration considered in this study surpasses this value, exceeding 18.4 dBi within the operating band. In terms of bandwidth, wave port-fed antenna demonstrates a significantly wider impedance bandwidth exceeding 3 GHz, compared to their 1.5 GHz. Regarding SLL, the sector beam antenna achieves a lower SLL of -20 dB, whereas the presented designs exhibit slightly higher values, ranging from -15 dB to -16.28 dB.

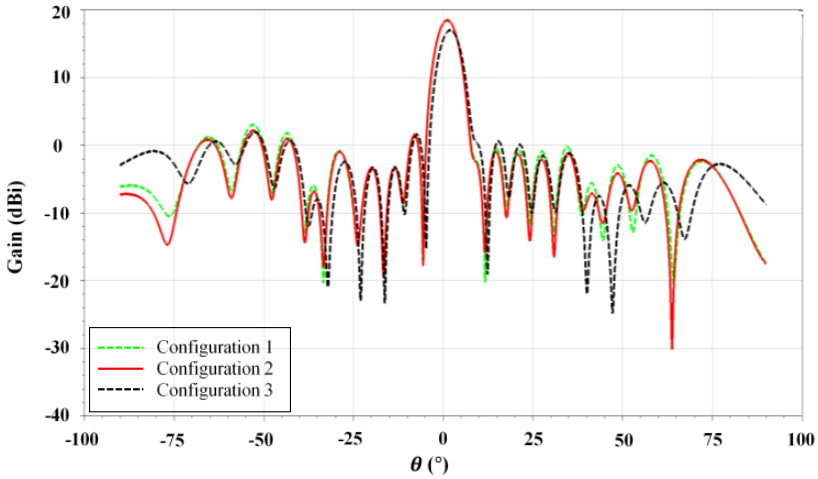

Figure 14. E-plane radiation patterns for the feed configurations.

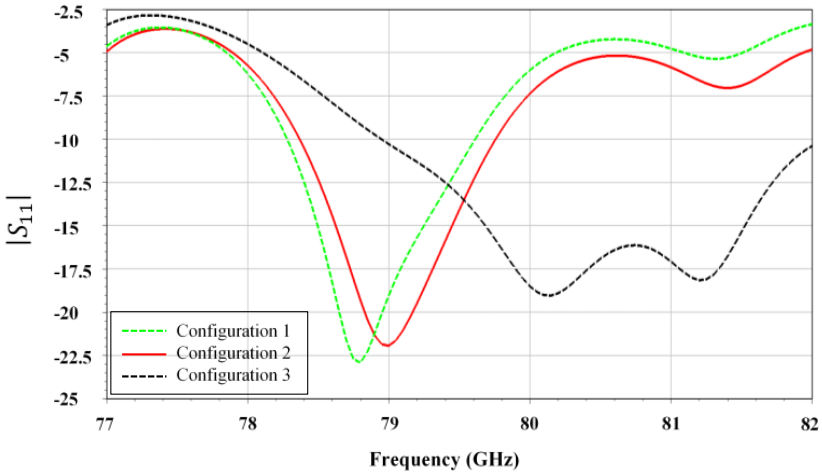

Figure 15. Simulated results of $|S_{11}|$ for the feed configurations.

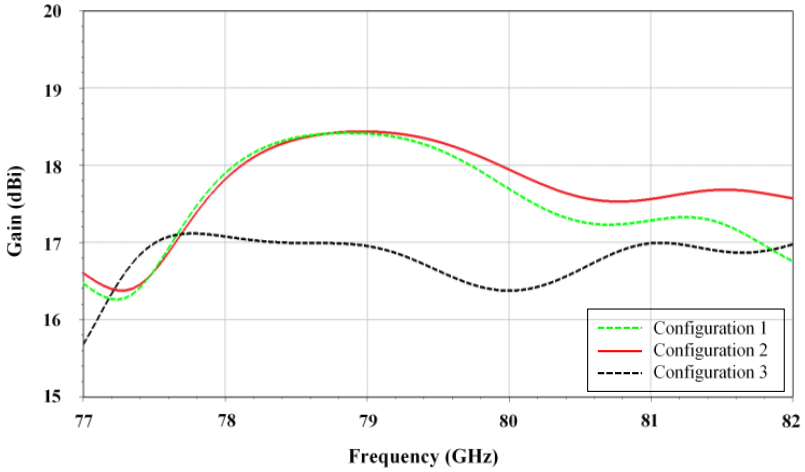

Figure 16. Gain results for the feed configurations.

Overall, the results achieved from the simulations are summarized in Table 4 to compare the key performance characteristics of the feed configurations.

Table 4. Comparison of the key performance characteristics of the antenna with the feed configurations.

Parameter	**Feed Configuration 1 & 2**	**Feed Configuration 3**
Impedance Bandwidth	∼1.4 GHz (similar to [30])	>3 GHz (higher than [30])
Frequency Shift	Minimal, well-aligned with 79 GHz	∼0.6 GHz shift toward higher frequency
Main Lobe Phase Centering (E-plane at 79 GHz)	$\theta = 1.1^{o}$ (closer to $\theta = 0^{o}$)	$\theta = 1.94^{o}$ (larger shift)
Directivity (Peak Gain)	Higher than [30], exceeding 18.4 dBi (as in [31])	Relatively high (17 dBi), but affected by frequency shift
Applicability for Automotive Radar	Better phase centering, strong gain performance	Wider bandwidth but potential frequency misalignment
Feed Network Complexity	Very lower than [30]	Medium
Fabrication Effort	Low	Moderate

The findings from the results highlight the trade-offs between bandwidth, frequency stability, and radiation pattern control when selecting port excitation methods for GCPW feed configurations. Moreover, the results also confirm that the antenna array with the GCPW feed configurations provides low reflection losses and high, stable gain within the 76–81 GHz automotive radar frequency band. The combination of a broad impedance bandwidth and high directivity could make this antenna a viable candidate for ADAS and autonomous vehicle sensing applications. Moreover, the SLL values observed from the simulations are relatively low, ranging from −15 dB to −16.28 dB. In fact, future optimizations may focus on enhancing the gain performance and further suppressing sidelobes to minimize interference in complex environments. In this context, recent studies have demonstrated that further sidelobe suppression can be achieved using advanced techniques such as more advanced Dolph-Chebyshev tapering techniques, non-uniform amplitude excitation, or alternative feed structures [23], [24], [28]. While these approaches offer improved radiation characteristics, their implementation typically increases design and fabrication complexity, particularly in series-fed linear arrays where precise amplitude control is difficult to realize. In the context of this study, a balance was maintained between sidelobe performance and structural simplicity. Nonetheless, such techniques are considered promising and may be explored in future work to further optimize the antenna design, especially in scenarios where sidelobe suppression is prioritized.

To further assess the practicality of the proposed configurations, additional comparison criteria including design complexity and fabrication effort can also be considered. Lumped port configurations (first two configurations) offer a significantly simpler design and are highly compatible with standard PCB fabrication processes. When compared to more elaborate designs such as those in [30], phase-tuning elements or advanced matching structures are not required in lumped port configurations. This results in reduced implementation cost and lower sensitivity to alignment errors. In contrast, the wave port-based configuration may involve more complex simulation and calibration steps, and its practical realization may necessitate careful alignment to ensure consistent excitation. Therefore, the use of lumped-port GCPW feeds is considered advantageous in terms of manufacturability and overall system simplicity.

Although this study is based solely on full-wave electromagnetic simulations, the fabrication and experimental characterization of the proposed antenna array are considered essential for future work. Such validation would provide empirical verification of the simulated performance, particularly in terms of gain, impedance bandwidth, and radiation characteristics at millimeter-wave frequencies. Furthermore, it would allow assessment of fabrication-induced deviations and confirm the practical feasibility of the designed feed

configurations. The simulation-based analysis presented in this study is intended to serve as a preliminary but crucial step toward the development of high-precision radar antennas for automotive applications.

7. Conclusion

In this study, a high gain 1 × 16 microstrip patch antenna array is adapted to operate at 79 GHz by implementing GCPW feed configurations, including coplanar gap source port, vertical ground bridge, and wave port. Simulations were performed to evaluate the performance of the antenna array with the considered feed configurations. A comparative analysis was then conducted for performance evaluation considering simulated reflection coefficient, gain, and radiation pattern characteristics. According to the results, the wave port feed demonstrated the best performance in terms of impedance bandwidth, achieving a bandwidth greater than 3 GHz over the frequency range of 78.95–82 GHz. In contrast, the antenna with coplanar gap source port and vertical ground bridge, which employ lumped ports, exhibited better main lobe phase centering, with a minor shift of $\theta = 1.1°$ in the E-plane radiation pattern at 79 GHz. Additionally, incorporating vertical ground bridge excitation provided to attain a maximum gain of 18.435 dBi while maintaining SLL below -16.28 dB in the E-plane at 79 GHz. We believe that the antenna array with different GCPW feed configurations presented in this study could contribute to enhancing feed accuracy prior to prototype fabrication, thereby improving overall design precision.

Acknowledgement

The authors have independently created, reviewed, and edited the content, taking full responsibility for the final publication. The authors confirm that no Generative AI was used in drafting this manuscript. However, ChatGPT (OpenAI) and Gemini (Google AI) were utilized to enhance its language and readability.

References

[1] Global status report on road safety 2018. Accessed: Apr. 11, 2023. [Online]. Available: https://www.who.int/publications-detail-redirect/9789241565684
[2] Derawi M, Dalveren Y, Cheikh FA. Internet-of-things-based smart transportation systems for safer roads. In: 2020 IEEE 6th World Forum on Internet of Things (WF-IoT); 02-16 June 2020; New Orleans, LA, USA: IEEE. pp. 1–4.
[3] Greenwood PM, Lenneman JK, Baldwin CL. Advanced driver assistance systems (ADAS): Demographics, preferred sources of information, and accuracy of ADAS knowledge. Transp Res Part F Traffic Psychol Behav 2022; 86: 131–150.
[4] Yeong DJ, Velasco-Hernandez G, Barry J, Walsh J. Sensor and sensor fusion technology in autonomous vehicles: A review. Sensors 2021; 21(6): 2140.
[5] Wang C, Wang X, Hu H, Liang Y, Shen G. On the application of cameras used in autonomous vehicles. Arch Comput Methods Eng 2022; 29(6): 4319–4339.
[6] Royo R, Ballesta-Garcia M, An overview of lidar imaging systems for autonomous vehicles. Appl Sci 2019; 9(19), 4093.
[7] Bilik I, Longman O, Villeval S, Tabrikian J. The rise of radar for autonomous vehicles: Signal processing solutions and future research directions. IEEE Signal Process. Mag. 2019; 36(5): 20–31.
[8] Bilik I, Comparative analysis of radar and lidar technologies for automotive applications. IEEE Intell Transp Syst Mag 2022; 15(1): 244–269.
[9] Li L, Ibanez-Guzman J. Lidar for autonomous driving: The principles, challenges, and trends for automotive lidar and perception systems. IEEE Signal Process Mag 2020, 37(4): 50–61.
[10] Patole SM, Torlak M, Wang D, Ali M. Automotive radars: A review of signal processing techniques. IEEE Signal Process. Mag. 2017; 34(2): 22–35.
[11] Bilik I, Bialer O, Villeval S, Sharifi H, Kona K, Pan M, Persechini D, Musni M, Geary K. Automotive MIMO radar for urban environments. In: 2016 IEEE Radar Conference (RadarConf); 02-06 May 2016; Philadelphia, PA, USA: IEEE. pp. 1–6.
[12] Isaacs O, Tabrikian J, Bilik I. Cognitive antenna selection for optimal source localization. In: 2015 IEEE 6th International Workshop on Computational Advances in Multi-Sensor Adaptive Processing (CAMSAP); 13-16 December 2015; Cancun, Mexico: IEEE. pp. 341–344.
[13] Vargas J, Alsweiss S, Toker O, Razdan R, Santos J. An overview of autonomous vehicles sensors and their vulnerability to weather conditions. Sensors 2021; 21(16): 5397, 2021.
[14] Wang X, Stelzer A, A 79-GHz LTCC patch array antenna using a laminated waveguide-based vertical parallel feed. IEEE Antennas Wirel Propag Lett 2013; 12: 987–990, 2013.
[15] Khan O, Meyer J, Baur K, Waldschmidt C. Hybrid Thin Film Antenna for Automotive Radar at 79 GHz. IEEE Trans Antennas Propag 2017; 65(10): 5076–5085.
[16] Saleem MK, Vettikaladi H, Alkanhal MAS, Himdi M. Lens antenna for wide angle beam scanning at 79 GHz for automotive short range radar applications. IEEE Trans Antennas Propag 2017; 65(4): 2041–2046.

[17] Alami WO, Sabir E, Brahim L. A H-slotted patch antenna array for 79 GHz automotive radar sensors. In: 2018 6th International Conference on Wireless Networks and Mobile Communications (WINCOM); 16-19 October 2018; Marrakesh, Morocco: IEEE. pp. 1–6.
[18] Arnieri E, Greco F, Boccia L, Amendola G. A reduced size planar grid array antenna for automotive radar sensors. IEEE Antennas Wirel. Propag. Lett. 2018; 17(12): 2389–2393.
[19] Mosalanejad M, Ocket I, Soens C, Vandenbosch GAE. Multilayer compact grid antenna array for 79 GHz automotive radar applications. IEEE Antennas Wirel Propag Lett 2018; 17(9): 1677–1681.
[20] Mosalanejad M, Ocket I, Soens C, Vandenbosch GAE. Wideband compact comb-line antenna array for 79 GHz automotive radar applications. IEEE Antennas Wirel Propag Lett 2018; 17(9): 1580–1583.
[21] Tian J, Liu C, Gu X. Proximity-coupled feed patch antenna array for 79 GHz automotive radar. J Eng 2019; 19: 6244–6246.
[22] Yoo S, Milyakh Y, Kim H, Hong C, Choo H. Patch array antenna using a dual coupled feeding structure for 79 GHz automotive radar applications. IEEE Antennas Wirel Propag Lett 2020; 19(4): 676–679.
[23] Mousavi SH, Pourzadi A, Nezhad-Ahmadi MR, Safavi-Naeini S. Wideband corporate center-fed antenna for 79GHz automotive radar application. In: 2021 IEEE 19th International Symposium on Antenna Technology and Applied Electromagnetics (ANTEM); 08-11 August 2021; Winnipeg, MB, Canada: IEEE. pp. 1–2.
[24] Wang Z, Yi H, Xia D, Li L, Double-layer broadband and wide beam microstrip array antenna for 79GHz automotive radar. In: 2021 13th Global Symposium on Millimeter-Waves & Terahertz (GSMM); 23-26 May 2021; Nanjing, China: IEEE. pp. 1–3.
[25] Aliakbari H, Mosalanejad M, Soens C, Vandenbosch GAE, Lau BK, 79 GHz multilayer series-fed patch antenna array with stacked micro-via loading. IEEE Antennas Wirel Propag Lett 2022; 21(10): 1990–1994.
[26] Le TH, Kaiser M, Ndip M, Koeszegi JM, Thomas T, Nallaweg O, Dreissigacker M, Tschoban C, Schneider-Ramelow M. 3D mold embedded pcb-based mimo antenna arrays for 79 GHz automotive radar. In: 2023 20th european radar conference (EuRAD); 20-22 September 2023, Berlin, Germany: IEEE. pp. 2–5.
[27] Su GR, Eric SL, Huayan J, Hsu PH, Sun JS, Chin KS. 79-GHz SIW slot-coupled patch antenna array with low cross polarization and wide beamwidth. J Electromagn Waves Appl 2023; 37(1): 38–52.
[28] Sun J, Wu L, Li R, Zhang X, Cui Y. A wideband cavity-slotted waveguide antenna for mm-wave automotive radar sensors. IEEE Antennas Wirel Propag Lett 2024; 23(12): 4758–4762.
[29] Sharma G, Kumar M. CPW-fed castle shaped dielectric resonator antenna for anticollision short range radar at 79 GHz. In 2024 Second International Conference on Microwave, Antenna and Communication (MAC); 04-06 October 2024, Dehradun, India: IEEE. pp. 1–4.
[30] Lee JH, Lee JM, Seo DW. Design and evaluation of a sector beam antenna for 79-GHz short-range radar sensors. IEEE Access 2025; 13: 39087–39095.
[31] Yan J, Wang H, Yin J, Yu C, Hong W. Planar series-fed antenna array for 77 GHz automotive radar. In: 2017 Sixth Asia-Pacific Conference on Antennas and Propagation (APCAP); 16-19 October 2017, Xi'an, China: IEEE. pp. 1–3.
[32] Hsu WT, Lin SL. Using FMCW in autonomous cars to accurately estimate the distance of the preceding vehicle. Int J Automot Technol 2022; 23(6): 1755–1762.
[33] Pozar D. Surface wave effects for millimeter wave printed antennas. In: 1983 Antennas and Propagation Society International Symposium; 23-26 May 1983; Houston, TX, USA: IEEE. pp. 692–695.
[34] Balanis CA. Antenna Theory: Analysis and Design. 3rd ed. Hoboken, NJ, USA: John Wiley & Sons, 2005.
[35] Visser HJ. Array and Phased Array Antenna Basics. West Sussex, England: John Wiley & Sons, 2005.
[36] Jian B, Yuan J, Liu Q. Procedure to design a series-fed microstrip patch antenna array for 77 GHz automotive radar. In: 2019 Cross Strait Quad-Regional Radio Science and Wireless Technology Conference (CSQRWC); 18-21 July 2019; Taiyuan, China: IEEE. pp. 1–2.
[37] Lee JH, Lee JM, Hwang KC. Series feeding rectangular microstrip patch array antenna for 77 GHz automotive radar. In: 2017 International Symposium on Antennas and Propagation (ISAP); 30 October 2017 - 02 November 2017; Phuket, Thailand: IEEE. pp. 1–2.
[38] Shang X, Ridler NM, Ding J, Geen M. Introductory guide to making planar S-parameter measurements at millimetre-wave frequencies. Accessed: Mar. 29, 2025. [Online]. Available: https://doi.org/10.47120/npl.9001
[39] Dong Y, Johansen TK, Zhurbenko V. Ultra-wideband coplanar waveguide-to-asymmetric coplanar stripline transition from DC to 165 GHz. Int J Microw Wirel Technol 2018; 10(8): 870–876.